Journal of Alloys and Compounds 656 (2016) 368–377

Contents lists available at ScienceDirect

Journal of Alloys and Compounds

journal homepage: http://www.elsevier.com/locate/jalcom

Synthesis and field electron emission properties of waste cooking palm oil-based carbon nanotubes coated on different zinc oxide nanostructures

A.B. Suriani [a, b, *], R.N. Safitri [a, b], A. Mohamed [a, c], S. Alfarisa [a, b], M.F. Malek [d, e], M.H. Mamat [e], M.K. Ahmad [f]

[a] Nanotechnology Research Centre, Universiti Pendidikan Sultan Idris, 35900 Tanjung Malim, Perak, Malaysia
[b] Department of Physics, Universiti Pendidikan Sultan Idris, 35900 Tanjung Malim, Perak, Malaysia
[c] Department of Chemistry, Faculty of Science and Mathematics, Universiti Pendidikan Sultan Idris, 35900 Tanjung Malim, Perak, Malaysia
[d] NANO-ElecTronic Centre (NET), Faculty of Electrical Engineering, Universiti Teknologi MARA (UiTM), 40450 Shah Alam, Selangor, Malaysia
[e] NANO-SciTech Centre (NST), Institute of Science (IOS), Universiti Teknologi MARA (UiTM), 40450 Shah Alam, Selangor, Malaysia
[f] Microelectronic and Nanotechnology–Shamsuddin Research Centre (MiNT-SRC), Faculty of Electrical and Electronic Engineering, Universiti Tun Hussein Onn Malaysia, 86400 Parit Raja, Batu Pahat, Johor, Malaysia

ARTICLE INFO

Article history:
Received 13 April 2015
Received in revised form
28 September 2015
Accepted 29 September 2015
Available online 3 October 2015

Keywords:
Carbon nanotubes
Zinc oxide
Composite material
Vapour deposition
Sol–gel processes
Field electron emission

ABSTRACT

Carbon nanotubes (CNTs) from waste cooking palm oil were synthesised on different zinc oxide (ZnO) nanostructures including nanorods (ZNRs), nanoflowers (ZNFs) and nanorods-nanoflakes (Al:ZNRs-FLs) via thermal chemical vapour deposition method. The ZnO nanostructures were controllably synthesised by sonicated sol–gel immersion method. The morphologies and crystal structures of the nanostructures were observed using field emission scanning electron microscopy, photoluminescence spectroscopy, X-ray diffractometer and micro-Raman spectroscopy. The diameter and density of CNTs were affected by the presence of ZnO nanostructures. Moreover, the morphology of ZnO nanostructures was modified during the synthesis of CNTs. The presence of ZnO reduced the barrier layer between CNTs and substrate, thus enhanced the field electron emission (FEE) properties of CNTs. Among the ZnO nanostructured prepared, the growth of CNTs on ZNFs gave the best FEE performance with the lowest turn-on field (0.8 V/μm at 1 μA/cm^2). The ZNFs trapped more iron (Fe) elements and promote the tip and body-emission processes in the sample. Moreover, the presence of Fe elements also reduced the work function of ZNFs/CNTs nanocomposite and acted as additional electrons. Therefore, the significant FEE performance enhancement was observed.

1. Introduction

In the recent years, studies on the electrical properties of carbon nanotubes (CNTs) have attracted much attention in view of their application in field electron emission (FEE) devices due to their high conductivity, high aspect ratio, high chemical and mechanical stabilities [1–7]. The shape-modification of CNTs with a low threshold electric field of 3.75 V/μm, high field emission current density of 1.6×10^{-5} A/cm^2 and good emission stability has been reported [8]. Extremely low turn-on and threshold fields of 0.33 and 0.48 V/μm respectively were obtained by fabricating CNTs yarn [9]. Nevertheless, low resistance at oxygen ambience [10] and weak bonding between CNTs and substrate [11] imposed the commercially available electron field emitter based on CNTs. Many attempts were conducted in order to improve the FEE performance of CNTs such as substrate and tip modifications [12], nitrogen plasma treatment [13] and deposition temperature controlling [14]. However, the presented methods are less effective in terms of cost and procedures since the sophisticated equipment and complex procedures are required.

Recently, the researchers have focussed their attention on the synthesis of carbon nanocomposites due to their improvement of excellent physical, chemical and mechanical properties [15–19]. Combination of metallic CNTs and semiconducting zinc oxide (ZnO)

---

* Corresponding author. Department of Physics, Universiti Pendidikan Sultan Idris, 35900 Tanjung Malim, Perak, Malaysia.
E-mail address: absuriani@yahoo.com (A.B. Suriani).

http://dx.doi.org/10.1016/j.jallcom.2015.09.277
0925-8388/

nanostructures led to the semiconducting/metallic heterojunction which was very useful in nanodevice applications. ZnO itself has become one of the intensive studied materials because of its special properties such as wide band gap (~3.37 eV), high conductivity, good electron mobility and large exciton binding energy (60 meV) [20]. As known that the carbon based nanostructure acted as an electron acceptor while the ZnO nanostructure served as electron donor, the combination of CNTs and ZnO resulted in adorable advantages [21]. Moreover, one dimensional ZnO nanorods (ZNRs) with high aspect ratio were also suitable as the direct template for the growth of tubular nanostructures [22]. Yan et al. [23] reported a notable effect in utilizing CNTs/ZnO nanocomposite as an emitter compared to those on pristine CNTs and ZnO. In their study, the turn-on field of CNTs/ZnO nanocomposite was 1.80 V/μm, much lower than pristine CNTs (2.80 V/μm) and ZnO (5.30 V/μm). Pan et al. also reported a lower turn-on field of CNTs (1.17 V/μm) after composited with ZnO [24]. The improvement of FEE performance with lower turn-on field and higher current emission were resulted due to a better ohmic contact between CNTs and ZnO [24,25]. Moreover, the presence of ZnO avoided the spot welding of CNTs at the nanometre contact area due to the local joule heating [23] as well as enhanced the adhesion between CNTs and the substrate [11,26]. The additional of CNTs into ZnO nanostructures was also reported to successfully enhance its FEE properties as well as facilitated the growth of ZnO nanoflowers (ZNFs) on ZNRs [27]. Table 1 presents the previous related works on the FEE study of nanocomposited ZnO and CNTs.

Furthermore, as the morphology of nanostructure influenced its FEE performance, the controlling of its morphology became a crucial aspect [31]. Diverse morphologies of ZnO nanostructures have been synthesised through gas and aqueous thermal deposition [32–37]. Among the presented methods, the use of aqueous-based synthesis process was simple, greener, relatively low temperature and pressure as well as less expensive. Moreover, through this approach, the morphology of ZnO nanostructures was easily tailored by controlling the deposition parameters such as temperature, pH, deposition time and molarity [38–40]. Comparison studies on FEE properties of different ZnO nanostructures, including ZnO nanowires, nanocones and microspheres [31] and balls, nunchakus and belts [41] have been reported and they showed significant distinction on FEE characteristics. However, direct comparison studies on the effect of different ZnO nanostructures/CNTs nanocomposites on their FEE properties are rarely reported. Previously, the growth of nanostructured ZnO/CNTs nanocomposites showed different FEE characteristics [42–44]. Therefore, the investigation on the deposition of CNTs grown on different ZnO nanostructures is still a challenge.

Here we report a comparative investigation on FEE properties of CNTs grown on ZnO nanostructures. For the first time, CNTs synthesised from waste cooking palm oil (WCPO) were grown on different morphology of ZnO which are ZnO nanorods (ZNRs), nanoflowers (ZNFs) and nanorods-nanoflakes (Al:ZNRs-FLs). Compared to the previous studies on the synthesis of nanocomposited ZnO and CNTs, this study offers a low cost and simpler technique to fabricate and enhance the field emission of ZnO/CNTs nanocomposites. The ZnO nanostructures were synthesised via sonicated sol–gel immersion method under several controlled modifications. Meanwhile, natural WCPO precursor was used for the synthesis of CNTs using thermal chemical vapour deposition (TCVD) method. The structural and optical properties of the samples were characterised and the emission properties were also investigated.

2. Experimental

The synthesis of ZnO/CNTs nanocomposites were conducted in multi-step deposition process involving deposition of seeded catalyst, growth of ZnO nanostructures via sonicated sol–gel immersion method and synthesising CNTs from WCPO by TCVD method. The overall deposition process is summarized in the flow chart as presented in Fig. 1.

2.1. Synthesis of ZNRs and ZNFs on magnesium zinc oxide seeded catalyst layer

Detail preparation for the growth of ZNRs and ZNFs on magnesium zinc oxide (MgZnO) seeded catalyst layer has been reported elsewhere [45]. The sol–gel was prepared by dissolving zinc acetate dihydrate ($Zn(CH_3COO)_2 \cdot 2H_2O$), magnesium nitrate hexahydrate ($Mg(NO_3)_2 \cdot 6H_2O$) and mono-ethanolamine (C_2H_7NO) into 2-methoxyethanol. The precursors were sonicated in ultrasonic water bath (Memmert, operate at 230 V, 50–60 Hz and 2000 W) for 30 min at 50 °C and stirred at room temperature for 2 h. MgZnO seeded catalyst was obtained via depositing the MgZnO solution on silicon (Si) substrate using spin coating method operated at 3000 rpm for 60 s. The ZNRs and ZNFs were then grown on MgZnO seeded catalyst layer. The ZnO solution was prepared by dissolving zinc nitrate hexahydrate ($Zn(NO_3)_2 \cdot 6H_2O$) and hexamethylenetetramine ($C_6H_{12}N_4$) (HMT) into deionized water. The ZnO precursor was also sonicated and stirred similar with the previous MgZnO solution. MgZnO-coated substrates were then immersed into ZnO solution by placing at the top, facing downward, to produce ZNRs and at the bottom of the solution, facing upward, to grow ZNFs. The synthesis was carried out for 4 h at 95 °C in water bath. The annealing process was then conducted at 500 °C for an hour.

2.2. Synthesis of Al:ZNRs-FLs on aluminium zinc oxide seeded catalyst layer

The preparation of Al:ZNRs-FLs on aluminium zinc oxide (AlZnO) seeded catalyst layer was similar as described elsewhere [46,47]. The aluminium nitrate nonahydrate ($Al(NO_3)_3 \cdot 9H_2O$) was added in sol–gel ZnO prepared from zinc acetate dihydrate, monoethanolamine, and 2-methoxyethanol. They were initially sonicated for 30 min at 50 °C, stirred and aged for 3 h at room temperature. The aluminium nitrate nonahydrate was also added as a dopant in the ZnO solution. The AlZnO-coated Si substrate was then immersed in the ZnO solution by placing at the bottom of the

Table 1
Previous related works on the FEE performances of nanocomposited ZnO and CNTs.

No.	Turn on field	Max. current density	References
1.	2.2 V/μm at 10 μA/cm^2	~340 μA/cm^2	Carbon/ZnO nanocomposites by CO_2 laser ablation by Kaushik et al. [21].
2.	2.8 V/μm at 10 μA/cm^2	~8 mA/cm^2	CNTs/ZnO heterojunction arrays by Yan et al. [23].
3.	2.8 V/μm at 1 mA/cm^2	~1 mA/cm^2	Surface fluorinated ZnO/CNTs by Wang et al. [25].
4.	3.7 V/μm at 10 μA/cm^2	~300 μA/cm^2	Highly stable field emission of ZnO/CNTs by Patra et al. [28].
5.	1.85 V/μm at 10 μA/cm^2	218 μA/cm^2	ZnO/CNTs composites via DC electrophoresis by Min et al. [29].
6.	0.31 V/μm at 10 μA/cm^2	N/A	ZnO/CNTs composites via microwave plasma jet CVD by Su et al. [30].
7.	4.6 V/μm at 1 μA/cm^2	~110 μA/cm^2	Enhanced field emission of ZnO grown on CNTs by Suriani et al. [27].

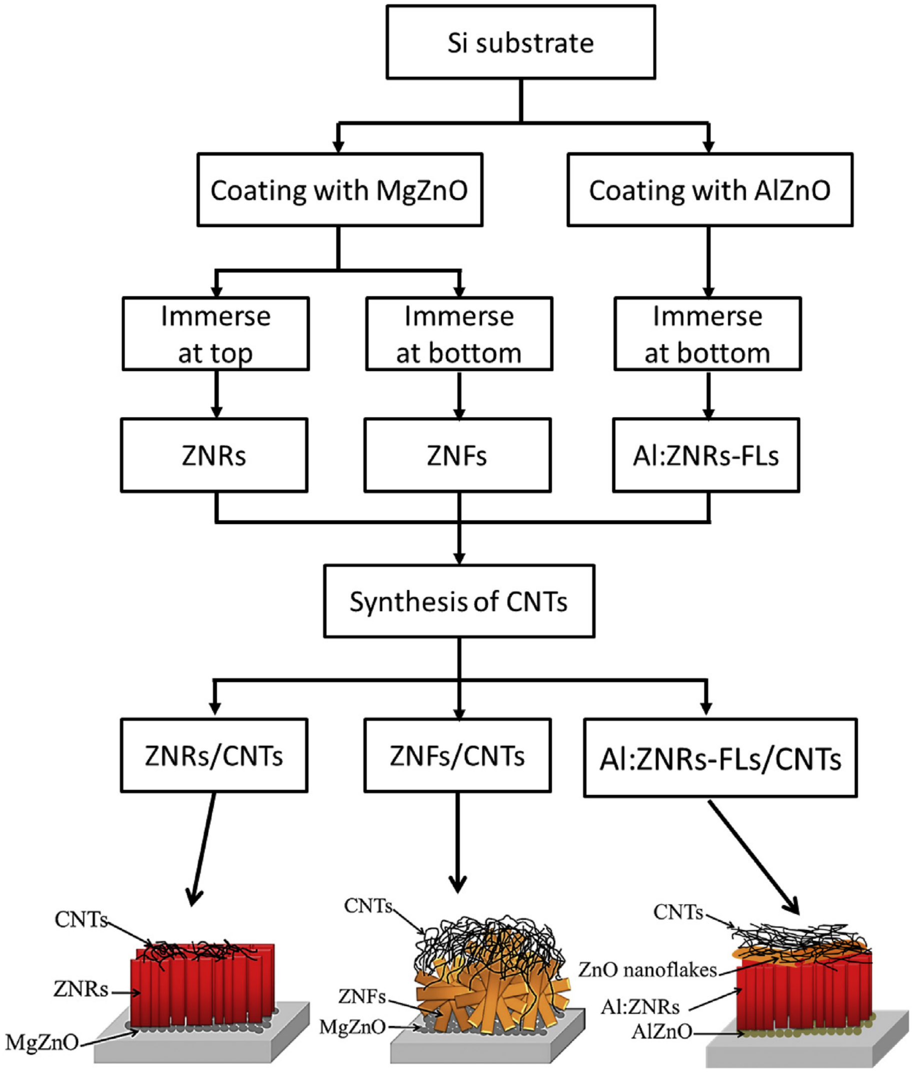

Fig. 1. The flow chart of ZnO/CNTs nanocomposites fabrication.

solution. The synthesis was also conducted at 95 °C for 4 h, followed by the annealing process for an hour at 500 °C.

2.3. Synthesis of CNTs on various ZnO nanostructures

CNTs were synthesised from WCPO in two-stage TCVD furnace following the previous works [48–51]. The as-grown ZnO nanostructures on Si substrate were placed in the synthesis zone and were heated at 750 °C. The WCPO mixed ferrocene as catalyst was loaded in precursor zone and it was heated at 450 °C. The synthesis was conducted for 30 min and another 30 min for annealing process.

2.4. Sample characterizations

The surface morphologies of the samples were observed using field emission scanning electron microscope (FESEM, Hitachi SU8020). The photoluminescence (PL) spectrum and X-ray diffraction (XRD) patterns of all prepared samples were recorded by Horiba Jobin Yvon spectrophotometer using He–Cd 325 nm and PANalytical X'Pert Pro, respectively. Structural properties of CNTs produced were studied using micro-Raman spectroscopy (Renishaw InVia Raman microscopy) and the composition of the samples was investigated using the energy dispersive X-ray (EDX, Horiba EMAX) spectroscopy. Furthermore, the emission properties of the samples were investigated using FEE equipment (Hewlett–Packard 34401A multimeter).

3. Results and discussion

FESEM images of all prepared samples are presented in Fig. 2. The ZNRs on MgZnO seeded catalyst in Fig. 2(a) has a vertical orientation with the hexagonal-tip shape width in the range of 59–200 nm. Low density and twisted CNTs were grown on the aligned ZNRs as shown in Fig. 2(b). The diameter of CNTs was observed in the range of 21.4–55.3 nm. From the side view observation (Fig. 2(c)), it can be seen that the entangled CNTs were grown on the aligned ZNRs. The modification of ZNRs nanostructures were also observed due to sublimation and partial desorption of zinc and oxygen [52].

The growth of ZNFs is shown in Fig. 2(d). The flower-like structure was observed to be composed by rod structures with the average diameter of 240 nm. The average rod diameter of ZNFs (240 nm) was larger than ZNRs (59–200 nm). This was due to the different position of substrate immersion in the ZnO solution. The precipitation of Zn-HMT complex mainly occurred at the bottom of

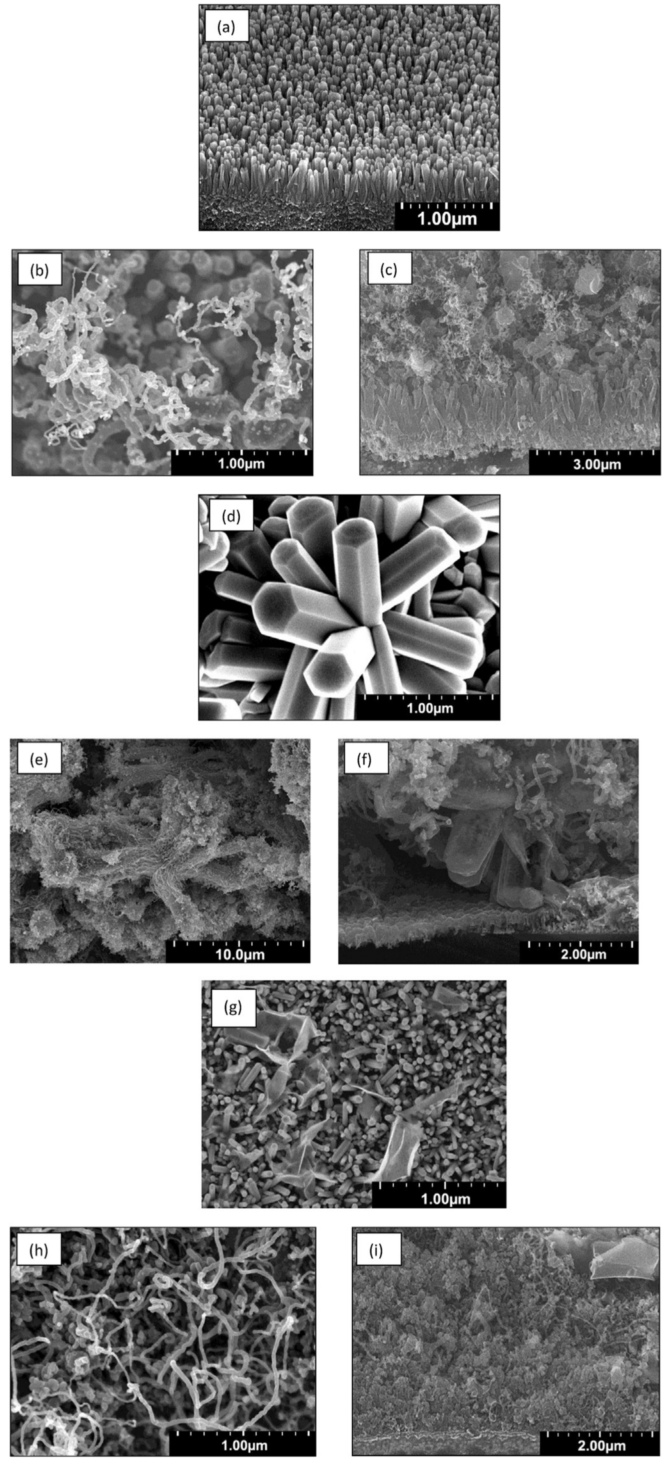

Fig. 2. FESEM images of (a) ZNRs, (b) top and (c) side view of ZNRs/CNTs, (d) ZNFs, (e) top and (f) side view of ZNFs/CNTs, (g) Al:ZNRs-FLs, (h) top and (i) side view of Al:ZNRs-FLs/CNTs.

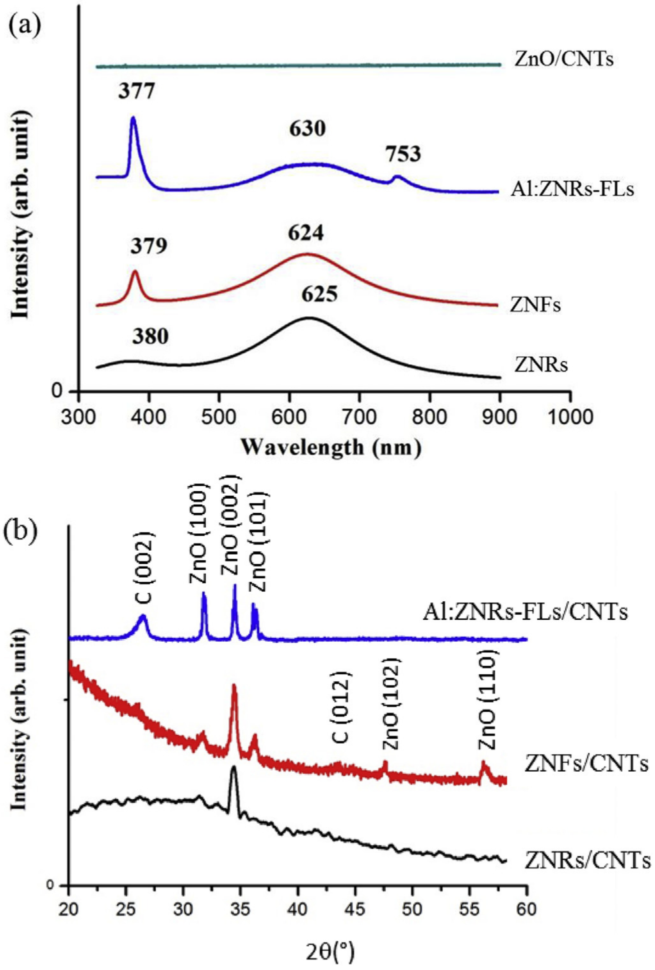

Fig. 3. (a) PL spectra, (b) XRD pattern of the samples.

the ZnO solution. Since the interfacial free energy of *c*-axis was higher than *a*-axis, the nanorods in this sample tended to horizontally grow and agglomerated to reduce its interfacial free energy [53]. Therefore, it resulted in larger formation of ZnO nanoparticles during the nucleation and thus produced flower-like structures with larger diameter. On the other hand, the CNTs grown on ZNFs (Fig. 2(e)) were denser than those on ZNRs. However, the diameter of CNTs was observed to be larger in the range of 30–60 nm (Fig. 2(f)). The growth of ZNFs left some empty spaces on the MgZnO seeded catalyst and it was suggested that the MgZnO also acted as an additional catalyst for the growth of CNTs [54]. Hence, denser and longer CNTs were obtained. The ZNFs also deformed after the deposition of CNTs as shown in Fig. 2(f), indicated the partial desorption of zinc and oxygen also occurred.

CNTs were also deposited on the Al:ZNRs-FLs. As shown in Fig. 2(g), the rod structures were observed to grow with diameter in the range of 30–85 nm and the flake structures were sequentially grown on top of the rod arrays with size around 226–559 nm. The CNTs were then grown on the Al:ZNRs-FLs structures as presented in Fig. 2(h). Dense CNTs were observed to have diameters ranging from 16.8 to 36.5 nm. Compared with the other nanocomposite samples, CNTs grown on Al:ZNRs-FLs possessed the highest density with the smallest diameter range. The as-grown CNTs covered the Al:ZNRs-FLs as observed from the side view observation (Fig. 2(i)). It was also predicted that the Al:ZNRs-FLs were modified after the deposition of CNTs.

In the mean times, based on the FESEM observation, it can be noticed that the diameter of ZnO nanostructures grown on AlZnO seeded catalyst layer was smaller than those on MgZnO seeded catalyst layer. The smaller radii of Al^{3+} (0.53 Å) than Mg^{2+} (0.72 Å) help to facilitate the formation of smaller ZnO diameter [55,56]. The growth of CNTs on ZNFs and Al:ZNRs-FLs were observed to be denser as compared to those on ZNRs. This indicated that the ZNRs

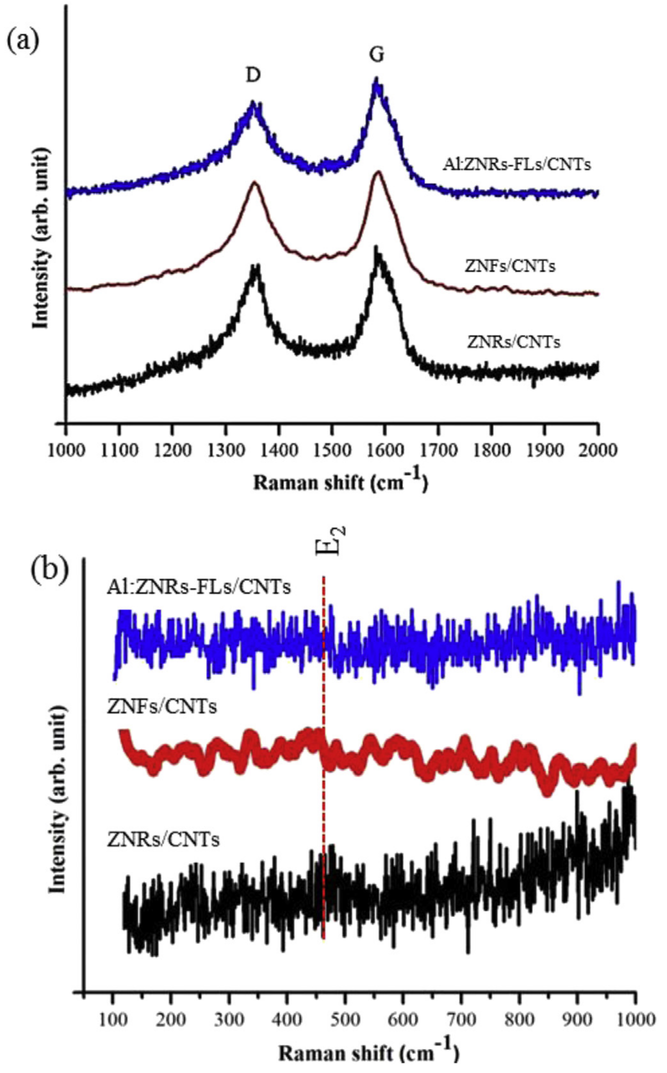

Fig. 4. Micro-Raman spectra of ZnO/CNTs nanocomposites with different Raman shift: (a) 1000–2000 cm^{-1}, and (b) 100–1000 cm^{-1}.

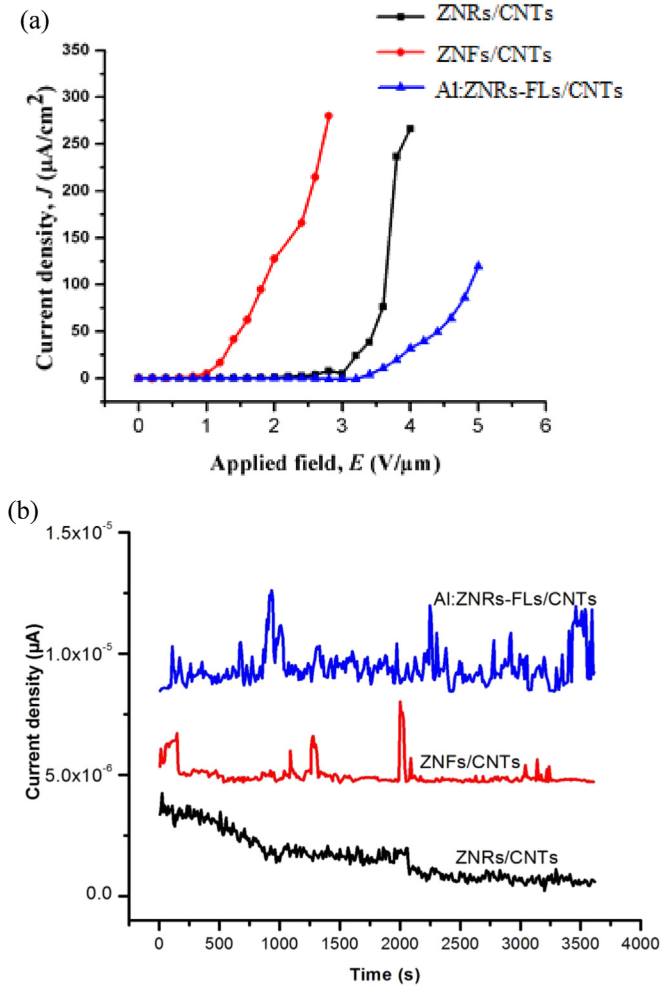

Fig. 5

Fig. 5. (a) J–E curves and (b) current stability of ZnO/CNTs nanocomposites.

have less catalytic activity because of the metastable-polar surface of aligned-orientation of ZNRs [57]. The heat introduced to synthesise CNTs sublimated the Zn, hence, the incoming iron (Fe), from ferrocene as the catalyst of CNTs, was proposed to substitute the sublimated Zn [58]. As a result, the Fe particles may less optimally catalyse the growth of CNTs. Even though the sublimation of Zn also occurred at the ZNFs, some empty spaces of ZNFs facilitated the MgZnO seeded catalyst to support the catalytic activity for the growth of CNTs [42]. The Al presented in Al:ZNRs-FLs was also believed to support the catalytic activity of CNTs, thus, resulted in smaller diameter and denser CNTs [59].

The PL observation was then conducted to study the defect level of produced ZnO nanostructures. Generally, the PL spectra of ZnO nanostructures at room temperature have two main peaks, ultraviolet (UV) and visible emission peaks. The UV emission (at around 370–380 nm) related to the free exciton recombination of near band edge transition and visible emission at around 620–630 nm indicated defect on the nanostructures [60]. Fig. 3(a) shows the PL spectra of the samples. The UV peaks for ZnO nanostructures were centred at 380, 379, and 377 nm for ZNRs, ZNFs, and Al:ZNRs-FLs respectively. These UV peaks were blue shifted which attributed to the quantum size confinement, as the diameter of rod-shape in ZNRs to Al:ZNRs-FLs was smaller [61]. The broad visible emission centred at red emission around of 625 nm indicated high defect level introduced in the ZnO nanostructures which may be attributed to transition from zinc interstitial (Zn_i) to oxygen interstitial (O_i) defect levels in ZnO [62]. Featureless PL spectra were observed for all ZnO/CNTs samples. The presence of CNTs on the as-grown ZnO nanostructures led to the absence of electron–hole recombination since the produced hole were filled by excited electron from another state, indicated that the as-grown CNTs were metallic-CNTs [63].

The XRD patterns of nanocomposites samples are depicted in Fig. 3(b). All the diffraction peaks in the XRD patterns can be indexed to the typical carbon and ZnO, and no impurities were detected. The typical graphite structures were obtained at 26 and 42° corresponded to (002) and (100) planes respectively [64]. Peaks originated from ZnO were detected at 2θ values of around 31, 34, 36, 47 and 58° assigned to (100), (002), (101), (102), and (110) respectively [64]. High intense peaks were presented by Al:ZNRs-FLs/CNTs sample which confirmed that the Al:ZNRs-FLs have the best crystal quality among the other ZnO/CNTs nanocomposite samples.

The quality of CNTs produced was studied from micro-Raman spectra as presented in Fig. 4(a). The characteristic peaks of CNTs were observed at around 1350 and 1590 cm^{-1} related to D and G

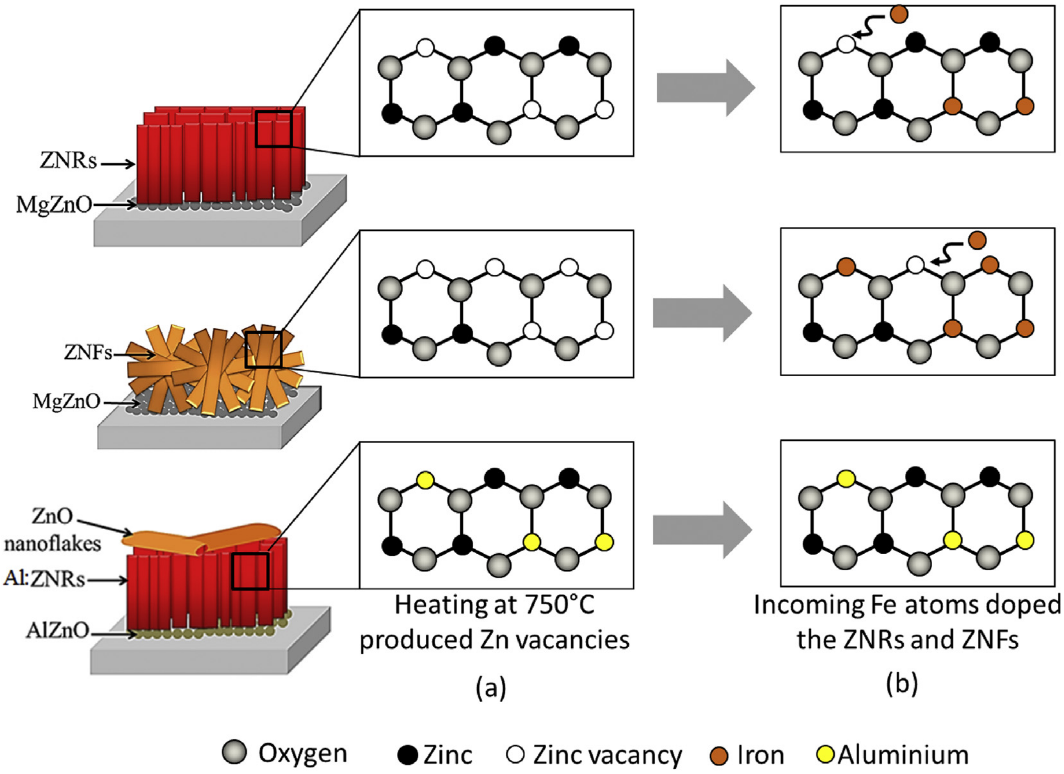

Fig. 6. The illustration of (a) formation of Zn vacancies due to high temperature and (b) the Fe doped ZnO.

band respectively. The I_D/I_G ratios of the CNTs grown on ZNRs, ZNFs and Al:ZNRs-FLs were found to be 0.89, 0.74 and 0.65 respectively. The highest I_D/I_G ratio was presented by ZNRs/CNTs sample which indicated that the ZNRs have less catalytic activity than the other nanostructure which then resulted in low quality of CNTs. On the other hand, the best quality of CNTs produced on Al:ZNRs-FLs was identified from the lowest I_D/I_G ratio. The vibrational peaks of ZnO nanostructures were hardly observed as the entire ZnO nanostructures were covered with CNTs. By magnifying the Raman spectra ranged from 100 to 1000 cm^{-1}, the E_2 mode of wurtzite phase hexagonal of ZnO was estimated to be 470, 452 and 456 cm^{-1} from the ZNRs/CNTs, ZNFs/CNTs and Al:ZNRs-FLs/CNTs samples respectively. Compared to the E_2 mode reported by Xu et al. [65], all the E_2 peaks in this study were blue shifted due to the diameter of ZnO nanostructures was bigger than the Bohr excitation radius of ZnO (2.3 nm) which resulted in optical confinement [66]. These might also be due to the anisotropic internal strength corresponded to interaction between CNTs and ZnO [67].

Fig. 5(a) shows the current density (J) as the function of applied field (E) of three different ZnO/CNTs nanocomposites. The turn-on and threshold fields are defined as the applied field at current densities of 1 and 10 $\mu A/cm^2$ respectively. Generally, the combination of CNTs and ZnO successfully enhanced the FEE properties of CNTs (the turn-on and threshold fields of pristine CNTs were 4.4 and 5.5 V/μm, respectively). The best FEE performance was presented by ZNFs/CNTs sample with the lowest turn-on and threshold fields of 0.8 and 1.1 V/μm, respectively. The ZNRs/CNTs have a moderate turn-on (2.3 V/μm) and threshold (3.3 V/μm) fields, while the lowest FEE performance was showed by Al:ZNRs-FLs/CNTs nanocomposite which possessed high turn-on and threshold fields of 3.3 and 3.6 V/μm, respectively. Previously, a double barrier-model for field emission of CNTs has been reported [11]. The first barrier is between substrate and CNTs and the second barrier is between CNTs and vacuum. By introducing ZnO between the substrate and CNTs, the covalent bond between CNTs and Zn was believed to reduce the first barrier, thus the electrons might pass the substrate-CNTs junction with lower obstacles [11,68]. Moreover, the presence of ZnO between substrate and CNTs was believed to enhance the adhesion of nanomaterial to the substrate [24] and release the joule heating produced during the emission process [69]. Therefore, it enhanced the FEE performances of CNTs with a stable current emission as presented in Fig. 5(b).

The different morphologies of ZnO nanostructures as an underlying growth of CNTs were observed to give different FEE characteristics. In this study, we proposed the role of Fe as the additional electron served in the emission process. As the heat introduced during the synthesis of CNTs (750 °C), the Zn sublimated from the ZnO and left the Zn vacancies (Fig. 6(a)) [58]. The incoming Fe atoms from the decomposition of ferrocene were believed to dope the ZNRs and ZNFs by filling the Zn vacancies (Fig. 6(b)) [70]. The ZNFs were believed to possess the highest surface area so that trapped the most Fe atoms as compared to other samples. This was revealed by EDX result that the Fe element content in ZNFs/CNTs sample was 6.77 at%. The EDX result also showed that the ZNRs/CNTs sample has 0.91 at% of Fe element which proposed that the Fe was diffused only at the tip of nanorods. The Fe doped ZnO was reported to decrease the energy gap (Eg) of ZnO [71]. Therefore, the electrons jumped from the valence to conduction band in short distance as the Eg was lowered by the presence of more Fe atoms. Moreover, the defect level originated from Fe doped affected the electrical conductivity of the samples [71]. By increasing the applied field during the FEE measurement, more charge carriers overcome the activation energy barrier and these carriers donated in the electron emission process. As the result, higher current density from the ZNFs/CNTs sample was produced (282.5 $\mu A/cm^2$ at applied field of 2.8 V/μm). Different condition was presented by Al:ZNRs-FL/CNTs sample which no Fe element detected by the EDX analysis. It was believed that the Zn

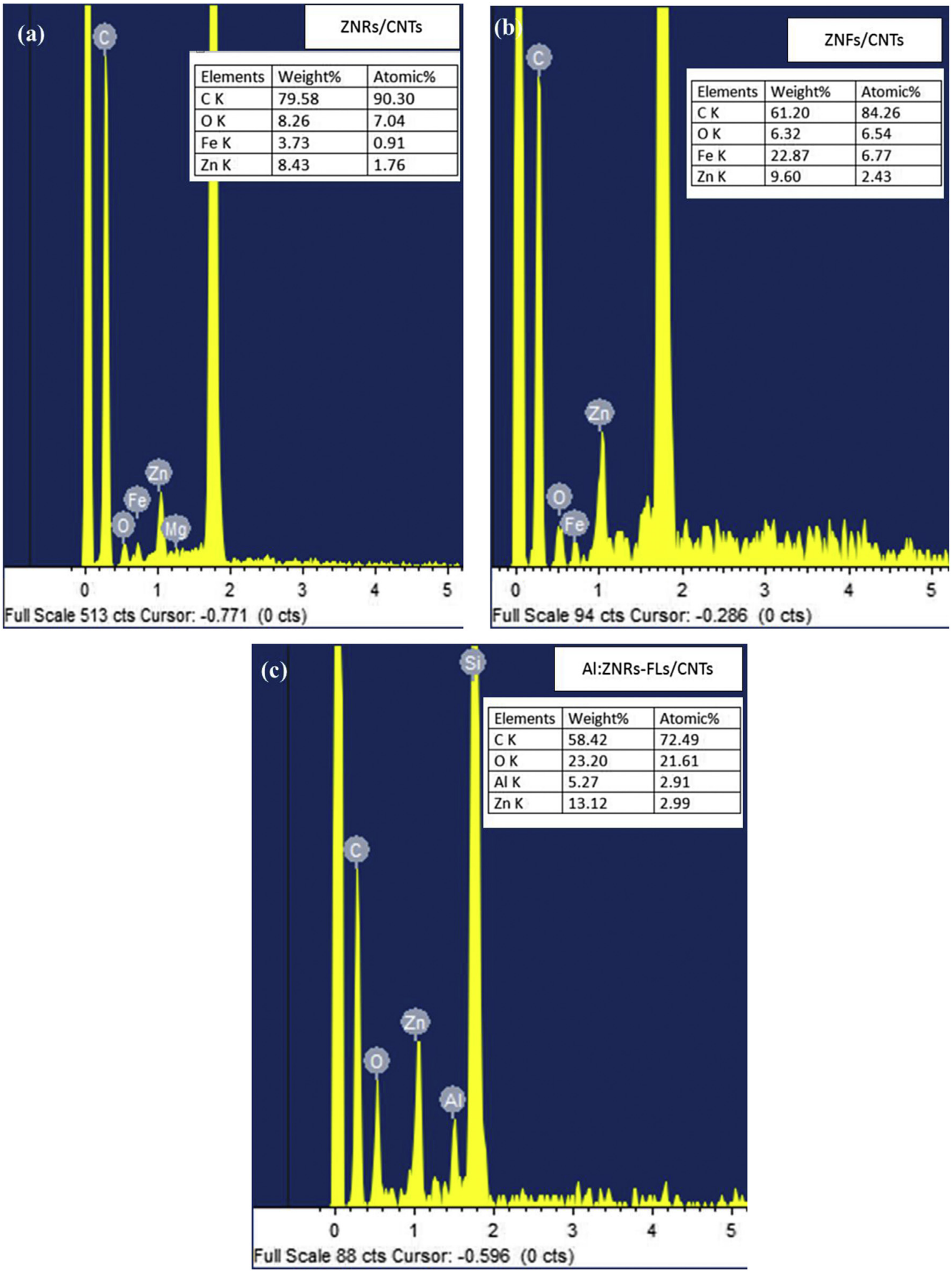

(a) ZNRs/CNTs

Elements	Weight%	Atomic%
C K	79.58	90.30
O K	8.26	7.04
Fe K	3.73	0.91
Zn K	8.43	1.76

(b) ZNFs/CNTs

Elements	Weight%	Atomic%
C K	61.20	84.26
O K	6.32	6.54
Fe K	22.87	6.77
Zn K	9.60	2.43

(c) Al:ZNRs-FLs/CNTs

Elements	Weight%	Atomic%
C K	58.42	72.49
O K	23.20	21.61
Al K	5.27	2.91
Zn K	13.12	2.99

Fig. 7. EDX analysis of ZnO/CNTs nanocomposites.

vacancies in the sample were fully filled by Al since the sample was initially doped with Al which led to the higher thermal and chemical stability [72,73]. Thus the Fe atoms have no possibility to diffuse into Al:ZNRs-FLs. Moreover, the presence of Al in the Al:ZNRs-FLs/CNTs sample caused a poor FEE performance since the Al and CNTs has a high contact resistance [11] (Fig. 7).

The sketched of band diagram of the samples is presented in Fig. 8. The growth of CNTs on Si substrate produced two barriers for electrons to be overcome during the emission process (Fig. 8(a)). The work function of ZnO, CNTs and ZnO/CNTs nanocomposite were reported to be 5.3, 5.0 and 5.15 eV respectively [23]. As the Fe-doped ZnO was introduced between the CNTs and substrate, the Fe–ZnO–C

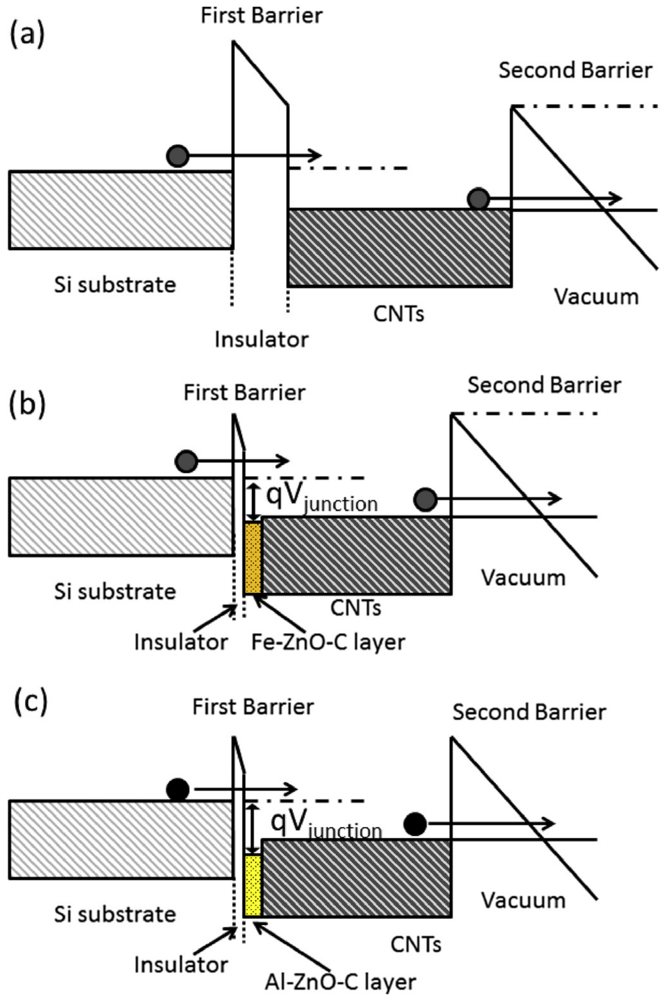

Fig. 8. Band structures of double-barrier model for FEE of (a) pristine CNTs, (b) ZNRs/CNTs and ZNFs/CNTs, and (c) Al:ZNRs-FLs/CNTs nanocomposites.

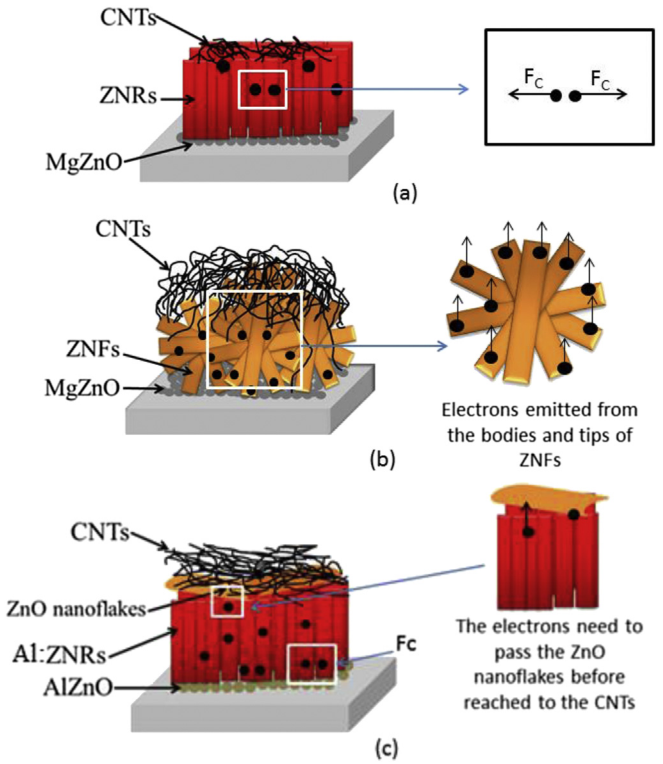

Fig. 9. Illustration of electrons transfer in (a) ZNRs/CNTs, (b) ZNFs/CNTs and (c) Al:ZNRs-FLs/CNTs nanocomposites.

conductive layer formed in the ZNRs/CNTs and ZNFs/CNTs samples, therefore reduced the first barrier as shown in Fig. 8(b). The work function of Fe was in the range of 4.0–4.7 eV, lower than the work function of ZnO and CNTs [74]. Previously, the presence of Fe was reported to lower the Eg of ZnO and work function of ZnO/CNTs [71]. As a result, the electrons would tunnel the junction with lowered obstacles. This condition also occurred in the Al:ZNRs-FLs/CNTs sample. The Al–ZnO–C conductive layer was also produced (Fig. 8(c)). A low work function of Al (work function of polycrystalline Al was reported to be 4.2 eV [75]) might reduce the work function of ZnO/CNTs nanocomposite. However, the Al was known to possess high contact resistance with CNTs [11]. Therefore, lower FEE performance was presented by the Al:ZNRs-FLs/CNTs sample.

The morphologies of ZnO nanostructures were also believed to give significant effect on the electrons transport in the samples. Generally, a high aspect ratio and vertically aligned-orientation of nanostructures gave beneficial effect on the FEE performance [42]. However, when the electrons moved in the ZNRs, at the closed distance between nanostructures, the Coulomb force (F_c) was generated by repelling each other. The repulsive force was directed parallel to the surface of the substrate and thus reduced the mobility of electrons that would be transferred to the CNTs [76]. This condition is illustrated in Fig. 9(a). Different condition was believed to occur in the ZNFs structures. The proper interspacing between the nanorods in the ZNFs structures was believed to reduce the F_c. Moreover, the body emission process was also believed to occur in the sample [77]. This larger emission site of ZNFs enables to emit more electrons from ZNFs to the CNTs side (Fig. 9(b)). Therefore, the best FEE performance was presented by ZNFs/CNTs sample. Fig. 9(c) illustrates the electrons transfer in the Al:ZNRs-FLs/CNTs sample. The Coulomb force was generated in the rod structures in this sample, similar to the rod-structures in ZNRs/CNTs sample, thus lowered the electrons mobility. Moreover, the presence of flake-structures in the sample generated additional barrier for electrons before reaching CNTs. Therefore, the lowest FEE performance was showed by Al:ZNRs-FLs/CNTs sample.

Based on the analysis, the difference of emission behaviour for ZnO/CNTs nanocomposites on various ZnO nanostructures could be summarized as below:

(1) The growth of CNTs on ZNRs facilitated the doping process of Fe in the ZNRs, thus resulted in Fe–ZnO–C conductive layer which reduced the barrier between CNTs and substrate. However, the closed distance between ZNRs was believed to generate a repel-F_C along the substrate. Therefore, lowered the electrons transfer from ZNRs to CNTs. As a result, a moderate FEE performance was presented by this sample.

(2) For ZNFs/CNTs nanocomposite sample, larger surface area of ZNFs provided large trapping side of Fe atoms hence, more Fe atoms were doped in the ZNFs. Thus, more effective Fe–ZnO–C conductive layer was generated in this sample. Moreover, the proper distance between nanorods in the flower-like structure was believed to reduce the repel-Coulomb force. Instead of tip emission process, body emission also occurred in this structure. Hence, more electrons were possibly transferred from ZNFs to CNTs. As compared to ZNRs/CNTs sample, the FEE performance in this sample improved.

(3) Meanwhile, the growth of CNTs on Al:ZNRs-FLs nanostructures was observed to give a poor FEE performance as compared to those on ZNRs and ZNFs. The presence of Al as a dopant in Al:ZNRs-FLs diminished the Fe doped process since the Zn vacancies were doped with Al. Even though the Al–ZnO–C conductive layer was proposed to form and reduced the barrier between CNTs and substrate, a high contact resistance between Al and CNTs was produced. The aligned nanorods structure in this sample also generated repel-F_C as presented in ZNRs/CNTs sample. Moreover, the presence of flake-structures was believed to give additional barrier for electrons before reaching CNTs. Thus, the lowest FEE performance was presented by Al:ZNRs-FLs/CNTs nanocomposite.

Finally, this investigation showed substantial role of ZnO on the FEE enhancement by improving the junction between CNTs and substrate. The role of Fe as the electron donor gave additional electrons during the emission process, thus resulted in higher maximum-current emission. Moreover, a low work function of Fe generated lower work function of ZNFs/CNTs nanocomposite as well as lowering the Eg of ZnO. Furthermore, the flower-shape of ZNFs also facilitated the body and tip-emission processes, hence enhanced the FEE properties with lower turn-on and threshold fields, higher-maximum current emission as well as stable current emission. Based on this study, the morphologies of ZnO nanostructures as an underlying growth of CNTs significantly affected the electron transfer in the sample. Therefore, the diversity of ZnO nanostructures opens up future studies on the ZnO/CNTs nanocomposites-based FEE.

4. Conclusion

CNTs were successfully synthesised on ZNRs, ZNFs, and Al:ZNRs-FLs via TCVD method from waste material namely WCPO. The diameter and density of CNTs produced were affected by the ZnO nanostructures. The growth of CNTs on Al:ZNRs-FLs possessed the highest crystalline quality with the lowest I_D/I_G ratio (0.65) of produced CNTs. However, the presence of Al in Al:ZNRs-FLs/CNTs nanocomposite resulted in high contact resistance with CNTs. Therefore, low FEE performance was showed. On the other hand, the maximum-trapped Fe in ZNFs successfully reduced the Eg of ZNFs and work function of ZNFs/CNTs as well as reduced the barrier layer between substrate and CNTs. Moreover, the proper distance between the nanomaterials of ZNFs assisted the body and tip-emission processes from ZNFs to CNTs. Therefore, the best FEE performance with lowest turn-on (0.8 V/μm) and threshold (1.1 V/μm) fields were presented by ZNFs/CNTs sample. This study showed that the morphology of nanostructures significantly affected their FEE properties.

Acknowledgements

The authors would like to thank the Research Acculturation Collaboration Effort (RACE-2012-0147-102-62) and Prototype Research Grant Scheme (PRGS:2013-0097-102-32) grants for financial supports and Universiti Pendidikan Sultan Idris.

References

[1] M. Miao, Carbon 49 (2011) 3755.
[2] I. Singh, D. Madhwal, A. Verma, A. Kumar, S. Rait, I. Kaur, L.M. Bharadwaj, C.S. Bhatia, P.K. Bhatnagar, P.C. Mathur, J. Lumin. 130 (2010) 2157.
[3] J.S. Choi, H.S. Lee, J.C. Goak, Y. Seo, K.B. Kim, Y.H. Song, Y.C. Choi, N.S. Lee, J. Alloys Compd. 521 (2012) 126.
[4] S. Ibrahim, R. Ahmad, M.R. Johan, J. Lumin. 132 (2012) 147.
[5] A.B. Suriani, A.R. Dalila, A. Mohamed, I.M. Isa, A. Kamari, et al., Mater. Res. Bull. 70 (2015) 524.
[6] A.B. Suriani, S. Alfarisa, A. Mohamed, I.M. Isa, A. Kamari, N. Hashim, M.H. Mamat, M. Rusop, Mater. Lett. 139 (2015) 220.
[7] A.B. Suriani, R.M. Nor, M. Rusop, J. Ceram. Soc. Jpn. 118 (2010) 963.
[8] Y.L. Zhang, L.L. Zhang, P.X. Hou, H. Jiang, L.I.U. Chang, H.M. Cheng, New Carbon Mater. 26 (2011) 52.
[9] J. Lee, Y. Jung, J. Song, J.S. Kim, G.W. Lee, H.J. Jeong, Y. Jeong, Carbon 50 (2012) 3889.
[10] H. Ham, G. Shen, J.H. Cho, T.J. Lee, S.H. Seo, C.J. Lee, Chem. Phys. Lett. 404 (2005) 69.
[11] J. Zhang, X. Wang, W. Yang, W. Yu, T. Feng, Q. Li, X. Liu, C. Yang, Carbon 44 (2006) 418.
[12] X. Yin, Q. Wang, L. Lou, X. Zhang, W. Lei, Appl. Surf. Sci. 254 (2008) 6633.
[13] B.B. Wang, Q.J. Cheng, X. Chen, K. Ostrikov, J. Alloys Compd. 509 (2011) 9329.
[14] J. Deng, Y. Yang, R. Zheng, G. Cheng, Appl. Surf. Sci. 25 (2012) 7094.
[15] M. Zhi, C. Xiang, J. Li, M. Li, N. Wu, Nanoscale 5 (2013) 72.
[16] J. Li, Z. He, C. Guo, L. Wang, S. Xu, J. Lumin. 145 (2014) 74.
[17] M. Kim, Y.C. Kim, Synt. Met. 198 (2014) 31.
[18] M.K. Mani, G. Viola, M.J. Reece, J.P. Hall, S.L. Evans, J. Alloys Compd. 601 (2014) 146.
[19] R.C. Wang, C.C. Hsu, S.J. Chen, Nanotechnol 22 (2011) 035704.
[20] F.V. Molefe, L.F. Koao, B.F. Dejene, Phys. B 439 (2014) 185.
[21] V. Kaushik, H. Sharma, A.K. Shukla, V.D. Vankar, Vacuum 106 (2014) 21.
[22] W. Gong, W. Chen, J. He, Y. Tong, C. Liu, L. Su, B. Gao, H. Yang, Y. Zhang, X. Zhang, Carbon 83 (2015) 275.
[23] X. Yan, B.K. Tay, P. Miele, Carbon 46 (2008) 753.
[24] J.Y. Pan, C.C. Zhu, Y.L. Gao, Appl. Surf. Sci. 254 (2008) 3787.
[25] H.Y. Wang, D.H. Chua, Appl. Surf. Sci. 265 (2013) 66.
[26] Y. Ling-min, F. Xin-hui, Q. Li-jun, Y. Wen, Appl. Surf. Sci. 257 (2011) 6332.
[27] A.B. Suriani, R.N. Safitri, A. Mohamed, S. Alfarisa, I.M. Isa, A. Kamari, N. Hashim, M.K. Ahmad, M.F. Malek, M. Rusop, Mater. Lett. 149 (2015) 66.
[28] R. Patra, S. Ghosh, H. Sharma, V.D. Vankar, Adv. Mater. Lett. 4 (2013) 849.
[29] Y.L. Min, Z.C. Chun, Appl. Surf. Sci. 255 (2009) 8359.
[30] C.H. Su, C.M. Huang, Mater. Lett. 111 (2013) 140.
[31] H. Jin, Y. Li, J. Li, C. Gu, Microelectron. Eng. 86 (2009) 1159.
[32] P.K. Baviskar, P.R. Nikam, S.S. Gargote, A. Ennaoui, B.R. Sankapal, J. Alloys Compd. 551 (2013) 233.
[33] F.V. Molefe, L.F. Koao, J.J. Dolo, B.F. Dejene, Phys. B Condens. Matter. 439 (2014) 185.
[34] F. Jamali-Sheini, R. Yousefi, Ceram. Int. 39 (2013) 3715.
[35] M.F. Malek, M.H. Mamat, Z. Khusaimi, M.Z. Sahdan, M.Z. Musa, et al., J. Alloy Cmpd. 582 (2014) 12.
[36] M.F. Malek, M.H. Mamat, M.Z. Musa, Z. Khusaimi, M.Z. Sahdan, et al., J. Alloy Cmpd. 610 (2014) 575.
[37] M. Salina, M. Rusop, A.B. Suriani, R. Ahmad, Trans. Electron Mater. 13 (2012) 64.
[38] D. Polsongkram, P. Chamninok, S. Pukird, L. Chow, O. Lupan, G. Chai, H. Khallaf, S. Park, A. Schulte, Phys. B Condens. Matter. 403 (2008) 3713.
[39] R. Shi, P. Yang, X. Dong, Q. Ma, A. Zhang, Appl. Surf. Sci. 264 (2013) 162.
[40] G. Amin, M.H. Asif, A. Zainelabdin, S. Zaman, O. Nur, M. Willander, J. Nano. Mat. 5 (2011).
[41] H. Hu, K. Yu, J. Zhu, Z. Zhu, Appl. Surf. Sci. 252 (2006) 8410–8413.
[42] C.S. Huang, C.Y. Yeh, Y.H. Chang, Y.M. Hsieh, C.Y. Ku, Q.T. Lai, Diam. Relat. Mater 18 (2009) 452.
[43] M. Seo, Y. Jung, D. Lim, D. Cho, Y. Jeong, Mater. Lett. 92 (2013) 177.
[44] Y.S. Min, E.J. Bae, U.J. Kim, W. Park, C.S. Hwang, Appl. Phys. Lett. 89 (2006) 113116–113121.
[45] M. Salina, A.B. Suriani, M.H. Mamat, R. Ahmad, M. Rusop, Adv. Mat. Res. 364 (2012) 35.
[46] M.H. Mamat, Z. Khusaimi, M.Z. Musa, M.Z. Sahdan, M. Rusop, Mater. Lett. 64 (2010) 1211.
[47] M.H. Mamat, Z. Khusaimi, M.Z. Musa, M.F. Malek, M. Rusop, Sens. Actuators A 171 (2011) 241.
[48] M.S. Azmina, A.B. Suriani, A.N. Falina, M. Salina, M. Rusop, Adv. Mater. Res. 364 (2012) 359.
[49] M.S. Azmina, A.B. Suriani, M. Salina, A.A. Azira, A.R. Dalila, et al., Nano Hybrids 2 (2012) 43.
[50] S.A.M. Zobir, S.A. Bakar, S. Abdullah, Z. Zainal, S.H. Sarijo, et al., J. Nanomater. 2012 (2012) 451473.
[51] A.B. Suriani, A.R. Dalila, A. Mohamed, M.H. Mamat, M. Salina, M.S. Rosmi, J. Rosly, M. Rusop, Mater. Lett. 101 (2013) 61.
[52] P. Mbuyisa, S.P. Bhardwaj, F. Rigoni, E. Carlino, S. Pagliara, L. Sangaletti, A. Goldini, M. Ndwandwe, C. Cepek, Carbon 50 (2013) 5472.
[53] L. Qi, H. Li, L. Dong, Mater. Lett. 10 (2013) 354.
[54] M. Salina, M.H. Mamat, S.A. Bakar, R. Ahmad, Y.M. Siran, S.A.M. Rejab, A.J. Asis, S. Tahiruddin, M. Rusop, Jpn. J. Appl. Phys. 50 (2011) 06GE02.
[55] J. Zhang, W. Que, Sol. Energy Mat. Sol. C 94 (2012) 2181.
[56] S.T. Lien, J.Z. Chen, Y.J. Yang, C.C. Hsu, I. Cheng, Ceram. Int. 40 (2014) 2707.
[57] Y. Xi, J. Song, S. Xu, R. Yang, Z. Gao, C. Hu, Z.L. Wang, J. Mater. Chem. 19 (2009) 9260.
[58] D. Lupu, A.R. Biris, F. Watanabe, Z. Li, E. Dervishi, V. Saini, Y. Xu, A.S. Biris, M. Baibarac, I. Baltog, Chem. Phys. Lett. 473 (2009) 299.
[59] P. Zarabadi-Poor, A. Badiei, A.A. Yousefi, B.D. Fahlman, A. Abbasi, Catal. Today 150 (2010) 100.

[60] R. Amiruddin, M.S. Kumar, J. Lumin 155 (2014) 149.
[61] N. Wang, Y. Yang, G. Yang, Nanoscale Res. Lett. 6 (2011) 1.
[62] A.B. Djurišić, Y.H. Leung, K.H. Tam, L. Ding, W.K. Ge, H.Y. Chen, S. Gwo, Appl. Phys. Lett. 88 (2006) 103.
[63] T. Koyama, K. Asaka, N. Hikosaka, H. Kishida, Y. Saito, A. Nakamura, J. Lumin. 131 (2011) 494.
[64] J. Klanwan, N. Akrapattangkul, V. Pavarajarn, T. Seto, Y. Otani, T. Charinpanitkul, Mater. Lett. 64 (2010) 80.
[65] C.X. Xu, X.W. Sun, Z.L. Dong, Y.P. Cui, B.P. Wang, Cryst. Growth. Des. 7 (2007) 541.
[66] A. Khan, J. Pak, Mater. Soc. 4 (2010) 5.
[67] D. Gültekin, M. Alaf, H. Akbulut, Acta. Phys. Pol. A 123 (2013) 275.
[68] C.C. Lin, B.T. Chu, G. Tobias, S. Sahakalkan, S. Roth, M.L. Green, S.Y. Chen, Nanotechnology 20 (2009) 1.
[69] H. Hirayama, Y. Kawamoto, Y. Ohshima, K. Takayanagi, Appl. Phys. Lett. 79 (2001) 1169.
[70] D. Karmakar, S.K. Mandal, R.M. Kadam, P.L. Paulose, A.K. Rajarajan, T.K. Nath, A.K. Das, I. Dasgupta, G.P. Das, Phys. Rev. B 75 (2007) 144404.
[71] C. Aydin, M.S.A. El-sadek, K. Zheng, I.S. Yahia, F. Yakuphanoglu, Opt. Laser Technol. 48 (2013) 447.
[72] I.H. Kim, D.Y. Ku, J.H. Ko, D. Kim, K.S. Lee, J.h. Jeong, T.S. Lee, B. Cheong, Y.J. Baik, W.M. Kim, J. Electroceram. 17 (2006) 241.
[73] Z. Zhan, J. Zhang, Q. Zheng, D. Pan, J. Huang, F. Huang, Z. Lin, Cryst. Growth Des. 11 (2011) 21.
[74] M. Kumar, T. Okazaki, M. Hiramatsu, Y. Ando, Carbon 45 (2007) 1899.
[75] D.R. Lide, Handbook of Chemistry and Physics, 73rd ed., C.R.C. Press, Boca Raton, 1992.
[76] J.A. Driscoll, B. Cook, S. Bubin, K. Varga, J. Appl. Phys. 110 (2011) 024304.
[77] G. Chai, L. Chow, Carbon 45 (2007) 281.